Cross-species brain circuitry from diffusion MRI tractography and mouse viral tracing

Siva Venkadesh[a,Ψ], Wen-Jieh Linn[b], Yuhe Tian[a], G Allan Johnson[c], Fang-Cheng Yeh[a]

[a] Department of Neurological Surgery, University of Pittsburgh, Pittsburgh, PA, USA.

[b] Department of Bioengineering, University of Pittsburgh, Pittsburgh, PA, USA.

[c] Duke Center for In Vivo Microscopy, Departments of Radiology and Biomedical Engineering, Duke University, Durham, NC, USA.

[Ψ]Correspondence: siv30@pitt.edu

Abstract:

We integrate tracer-derived projection polarity from ~1,200 mouse injections with species-specific diffusion MRI (dMRI) tractography to construct directed connectomes for mouse, marmoset, rhesus macaque, and human. We model brain circuitry as a directed connectome, in which asymmetric pathways capture the forward flow of neuronal signals. Using a common cross-species atlas as a scaffold, we introduced a multi-objective path efficiency metric that weighs projection strength against axonal length and applied directed shortest-path algorithms to quantify inter-regional influence. This framework revealed both conserved and divergent organization: the entorhinal–hippocampal projection remained the most efficient in all species, while humans exhibited strengthened temporal–insula–frontal circuits and reduced olfactory influence, rhesus macaques showed peak efficiencies in inferior temporal outflows, and marmosets maintained high olfactory influence. Together, these results establish a scalable approach for constructing directed connectomes across species and demonstrate how conserved and lineage-specific circuits jointly shaped association and sensory systems.

1. Introduction:

Comparative neuroscience seeks to identify how large-scale communication pathways are conserved across species and how they have been reallocated to support lineage-specific functions. A central requirement for this endeavor is the ability to reconstruct directed networks. Applications of graph theory and dynamical systems models of network function depend critically on projection polarity, because the influence one region exerts on another depends on the direction of signal transmission. Viral tract-tracing provides gold-standard evidence for directionality but is restricted to small-brain organisms such as the mouse[1]. In contrast, diffusion MRI (dMRI) enables whole-brain mapping in primates and humans but yields inherently bidirectional estimates that obscure true projection asymmetries[2–4]. This methodological disconnect has limited our ability to test how conserved communication pathways coexist with lineage-specific specializations in association, sensory, and limbic systems.

Building on a previously developed common hierarchical atlas, we combined the complementary strengths of viral tract-tracing and diffusion MRI. Viral tracing in the mouse brain, based on ~1,200 anterograde injection experiments[1], provides high-resolution, empirically validated directional polarity of axonal projections, while dMRI offers whole-brain coverage in humans and primates without directional specificity. By combining tracer-derived directionality with species-specific dMRI tractography, we constructed directed structural connectomes for each species. Brain circuitry, defined as the organized pathways supporting the forward flow of neuronal signals, is represented here as a directed connectome, a network in which inter-regional connections are modeled as asymmetric edges. We then quantified inter-regional influence using path efficiency, a novel multi-objective effective connection cost that favors shorter axons with stronger projections, reflecting the physical and metabolic investment per unit of potential influence.

Directed shortest-path algorithms[5] were applied to these networks, with results normalized for brain size and network scale to enable cross-species comparison.

Our analysis revealed both conserved pathways and lineage-specific reallocations in cortical communication. Across all species, the entorhinal–hippocampal projection ranked as the most efficient, underscoring the evolutionary preservation of memory-related circuitry. In humans, directed paths involving the anterior insula and superior temporal cortex showed pronounced efficiency gains, highlighting a strengthened temporal–insula–frontal circuit central to multimodal integration and language-related functions. In rhesus, inferior temporal outflows peaked, consistent with ventral visual stream specialization, while in marmosets, olfactory influence remained prominent relative to other primates. Together, these findings highlight conserved entorhinal–hippocampal circuits and divergent association and sensory pathways across species, enabled by directionally informed connectomics within a common atlas scaffold.

2. Results

We leveraged a recently developed common cross-species atlas[6] as the anatomical scaffold to integrate mouse viral tracing with diffusion MRI tractography and to generate cross-species brain circuitry (Fig. 1).

2.1. Cross-Species Directed Connectomes and Effective Cost Analysis

We first validated the integration of viral tracing and diffusion MRI tractography in the mouse before extending the framework to construct directed connectomes across species. In the mouse, individual viral tracer injections covered on average ~50% of an Allen Brain Atlas (ABA) ROI (Fig. 2a, left), underscoring the value of tractography for achieving near-complete sampling of white-matter projections. Tractography constrained with tracer-defined projection endpoints reproduced >90% of seed-only tracts, whereas random endpoints yielded far fewer matches (Wilcoxon signed-rank, $p \ll 0.0001$; Fig. 2a, right), confirming strong cross-modal correspondence, consistent with a prior report[7].

Whole-brain dMRI tractography[8] across mouse, marmoset, rhesus macaque, and human revealed pronounced species differences in scale and complexity (Fig. 2b). By integrating tracer-derived projection polarity with species-specific axonal lengths, we generated directed connectivity matrices of effective connection cost (Fig. 2c). This metric is biologically grounded: it reflects the

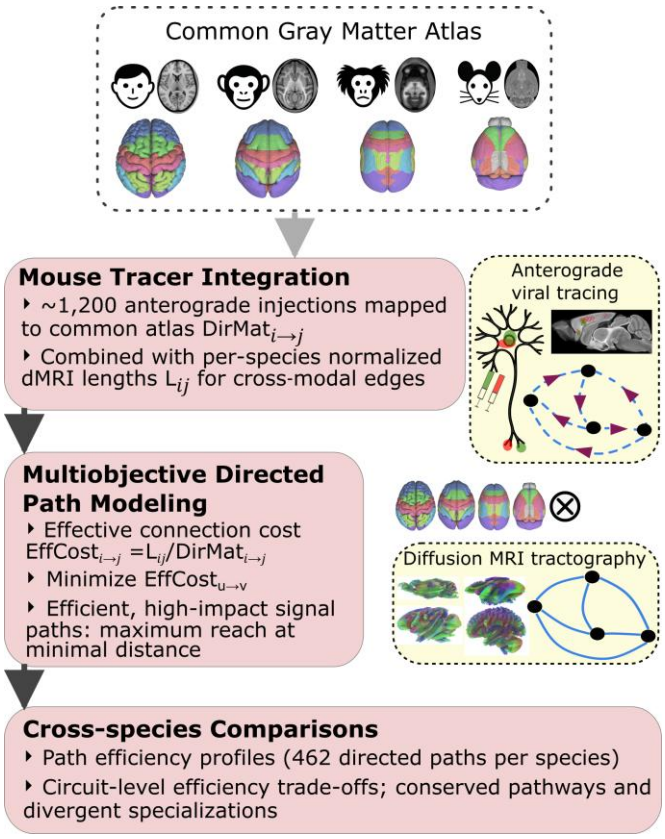

Figure 1 | Viral tracing–tractography integration for cross-species directed connectomes. Mouse viral tracer data provide projection polarity, which is mapped to a common atlas scaffold and combined with species-specific diffusion MRI to generate directed connectomes. Multi-objective path efficiency modeling is then applied to these networks to quantify inter-regional influence and enable systematic cross-species comparison.

physical and metabolic investment required for action potential propagation, favoring shorter axons with stronger projections as lower-cost routes of potential influence. In this formulation, the shortest directed paths correspond to minimal-cost sequences of axonal projections and synaptic relays through which neuronal signals are most likely to travel. Using this approach, we found that real connectomes exhibited lower mean path costs than degree- and weight-preserving null networks with randomized tracer-defined directionality (Fig. 3a, left). Directionality stabilized network organization: when randomized, networks admitted inefficient detours and spurious shortcuts, producing extreme outliers and inflated path costs (Supplementary Fig. 1).

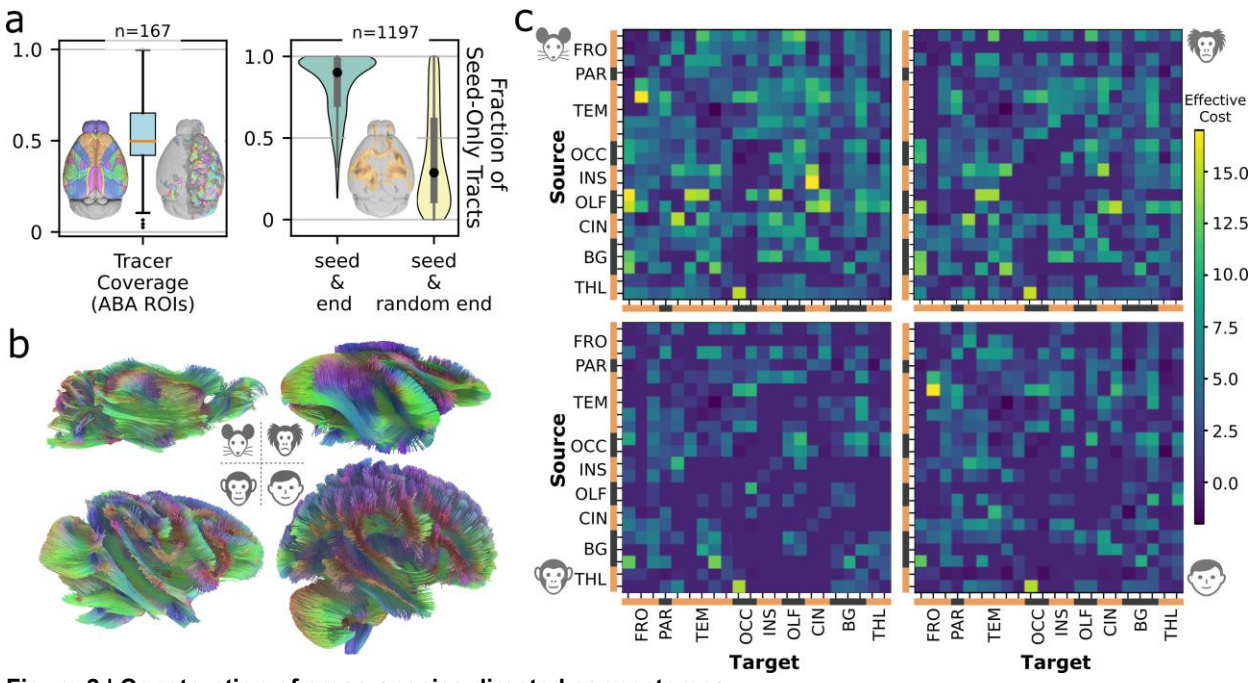

Figure 2 | Construction of cross-species directed connectomes.
(a) Left: Distribution of tracer coverage across Allen Brain Atlas (ABA) regions, with an average of ~50% coverage; inset shows ABA parcellation and viral injection sites. Right: Fraction of seed-only tracts reproduced when tractography was constrained with true tracer-defined projection endpoints versus random endpoints. Wilcoxon signed-rank test (one-tailed, "greater"): W = 680,071, $p \ll 0.0001$, $r = 0.80$ (large effect).
(b) Whole-brain tractography reconstructions for mouse, marmoset, rhesus macaque, and human brains.
(c) Directed connectivity matrices showing normalized effective connection costs for the four species, derived by integrating tracer-defined projection polarity with diffusion MRI tractography.

Effect-size comparisons highlighted a pronounced human advantage: path costs were lower in humans relative to mouse ($d = 0.61$), marmoset ($d = 0.75$), and rhesus macaque ($d = 0.70$) (Fig. 3a, right). Marmosets exhibited higher costs than both humans and rodents, likely due to constraints from longer axonal trajectories and less optimized routing in smaller primates. Rhesus macaques showed intermediate values. These cross-species differences suggest that evolutionary reorganization of network architecture may have restored and enhanced efficiency in humans despite expanded brain size.

Path-level analyses further revealed both conserved and divergent influence channels. Most notably, the medial temporal → hippocampus projection consistently ranked as the single most efficient pathway in all species (Fig. 3b), underscoring the evolutionary preservation of memory-related circuits[9,10]. Several additional high-efficiency routes in mouse, including occipital ↔ thalamus and premotor ↔ precentral pathways, were also highly ranked in primates, reflecting broader conservation across cortical and subcortical systems.

At finer scale, analyses within the Allen Brain Atlas (ABA) provided a cross-scale validation of the framework in mouse (Fig. 3c). In addition to recovering the canonical hippocampal trisynaptic circuit—including the perforant path[11] (ENTm → DG), mossy fibers[12] (DG → CA3), and Schaffer collaterals[13] (CA3 → CA1)—the ABA analysis also refined macro-scale connections represented in the common atlas, such as reciprocal LGd ↔ VISp interactions (thalamo–occipital) and MOp ↔ SSp_ll pathways (precentral–somatosensory).

Together, these results show that integration of tracer-derived directionality with species-specific tractography recovers the network's most influential channels across scales. Even when applied to a coarser cross-species atlas, the framework aligned with finer pathways defined in the ABA, supporting the biological fidelity of the integration approach for comparative analysis.

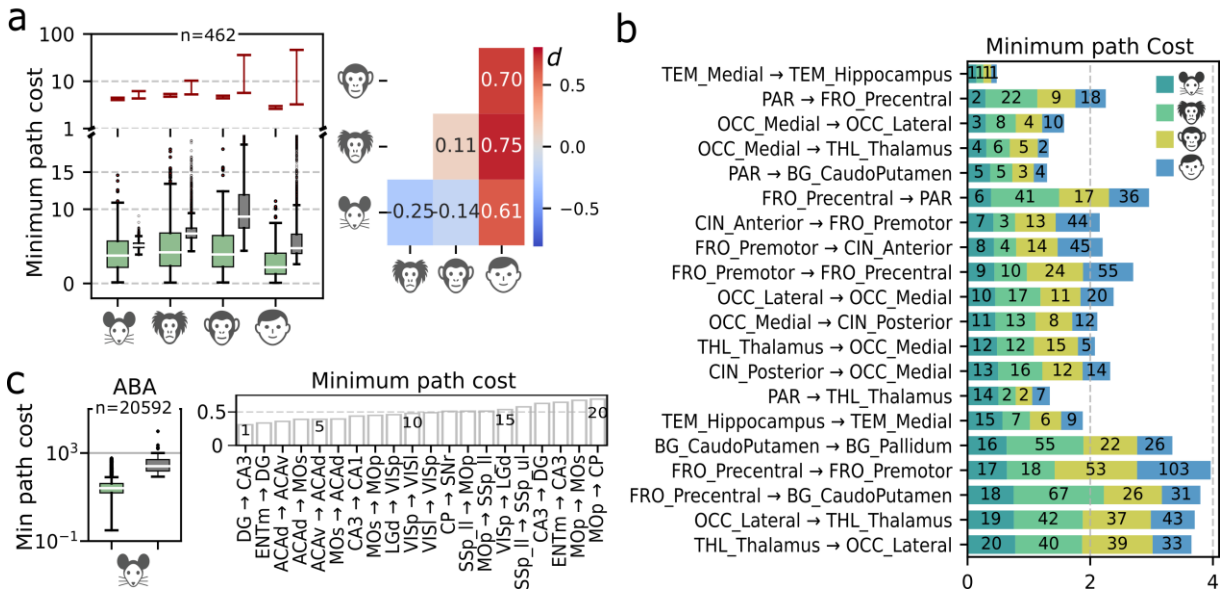

Figure 3 | Comparative analysis of directed path costs across species.
(a) Left: Path cost distributions for real connectomes (green) compared to null networks generated from 10,000 tracer-directionality permutations (gray). Broken y-axis provides an expanded range to display 95% confidence intervals of means (red bars). Right: Interspecies comparisons summarized by Cohen's *d*, with bootstrap *p*-values from 1000 resampling (Mouse vs Marmoset: $p<0.0001$; Mouse vs Rhesus: $p=0.0410$; Mouse vs Human: $p<0.0001$; Marmoset vs Rhesus: $p=0.0840$; Marmoset vs Human: $p<0.0001$; Rhesus vs Human: $p<0.0001$). Supplementary Fig. 1 provides additional details.
(b) Stacked bar plots showing the top 20 most efficient mouse paths (sorted by efficiency). Each bar displays the corresponding path cost for that same path in the mouse (base segment) and in the other three species (stacked segments). Path ranks in each species are annotated on the bars.
(c) Path cost analysis repeated at a finer spatial scale using the ABA atlas for the mouse. Left: Distribution of all possible path costs between ABA-defined regions (green) and in corresponding shuffled connectomes (gray). Right: Bar plot showing the costs of the top 20 most efficient ABA-defined mouse paths (sorted by efficiency), with path ranks annotated.

2.2. Regional, Role-Specific Cross-Species Differences in Path Efficiency

Having established whole-network efficiency profiles and their cross-scale validation, we next asked where efficiency reallocations were concentrated at the level of specific regions and roles. For each region, paths were grouped by whether it served as a source (outflow) or target (inflow), and efficiency distributions were compared across species. Six region–role combinations showed significant cross-species differences after FDR correction (Table 1).

The most consistent human gains occurred in the anterior insula (source and target) and superior temporal cortex (source), both showing elevated path efficiencies relative to other species (Fig. 4a). Partner-level Δ-connectomes clarified the basis of these effects (Fig. 5). Superior temporal outflows followed a stepwise trajectory: mouse and marmoset showed comparable levels, with increases emerging in rhesus and further amplified in humans. Stronger connections were observed to insula, thalamus, and prefrontal partners; the full temporal–insula–prefrontal circuit was most evident in the human–mouse comparison, while temporal–insula gains dominated in human–primate contrasts. Anterior insula efficiencies were lower in marmoset than mouse, but rose in rhesus and reached their highest values in humans. Insula inflows were stronger from superior temporal, hippocampal, and amygdalar partners, while insula outflows were stronger to temporal and hypothalamic partners. Together, these findings suggest that temporal–insula reciprocity is a consistent hallmark of human amplification across comparisons, with prefrontal participation emerging most clearly in the human–mouse contrast.

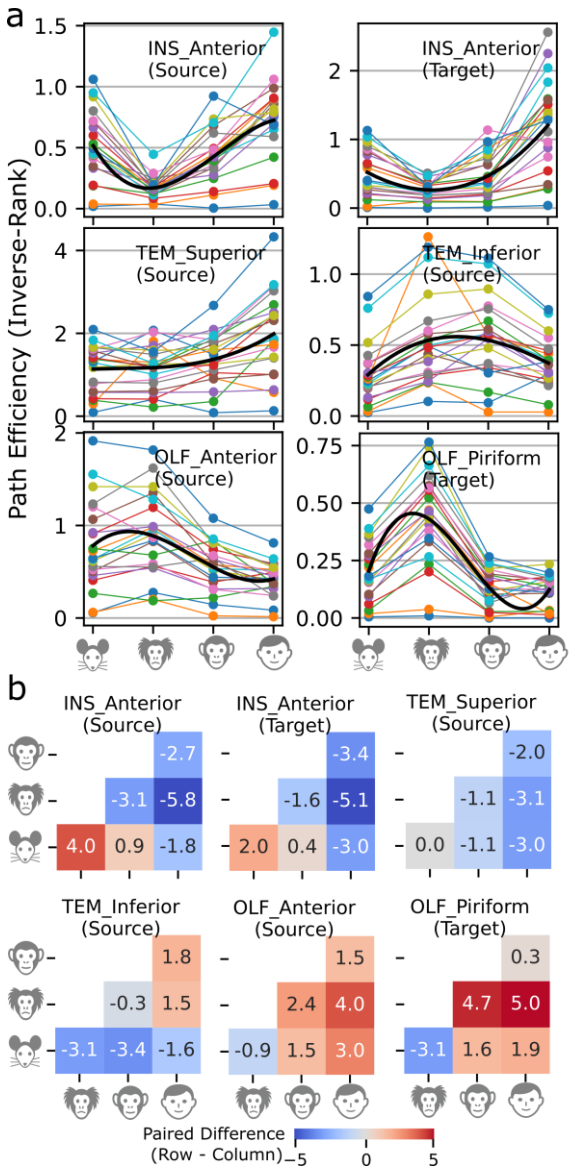

Figure 4 | Regional and role-specific distributions of path efficiency.
(a) Distributions of path efficiency for regions treated as sources (outflows) or targets (inflows), shown for mouse, marmoset, rhesus macaque, and human. Thin lines represent individual paths across species; thick black curves show the smoothed mean. Six region–role combinations showed significant cross-species differences after FDR correction (Table 1).
(b) Pairwise species comparisons (Dunn's post hoc tests; Supplementary Table 2). Negative values in the human column indicate higher efficiency in humans relative to the row species. Human gains are most pronounced for anterior insula and superior temporal roles, rhesus maxima appear in inferior temporal outflows, and marmoset maxima occur in olfactory inflows and outflows.

Table – 1. Regional-Level Cross-Species Comparisons Using Kruskal–Wallis Tests

Common Regions	As Source		As Target	
	Diff	*P*	*Diff*	*P*
FRO_Precentral	3.49	0.788	1.33	0.998
FRO_Premotor	0.74	0.998	2.53	0.899
FRO_Prefrontal	0.80	0.998	0.33	0.998
PAR	0.22	0.998	0.54	0.998
TEM_Superior	**12.41**	0.045	4.85	0.537
TEM_Inferior	**14.28**	0.022	7.63	0.199
TEM_Medial	0.90	0.998	0.35	0.998
TEM_Hippocampus	3.73	0.788	0.51	0.998
TEM_Amygdala	5.59	0.419	1.40	0.998
OCC_Lateral	0.18	0.998	0.10	0.998
OCC_Medial	0.36	0.998	0.08	0.998
INS_Anterior	**34.99**	0.000	**26.72**	0.000
INS_Posterior	5.64	0.419	0.73	0.998
OLF_Anterior	**18.10**	0.005	9.80	0.089
OLF_Piriform	11.63	0.055	**30.94**	0.000
CIN_Anterior	3.35	0.788	1.97	0.998
CIN_Posterior	0.04	0.998	0.24	0.998
BG_CaudoPutamen	3.40	0.788	0.86	0.998
BG_Accumbens	8.93	0.121	9.91	0.089
BG_Pallidum	2.74	0.899	2.57	0.899
THL_Thalamus	0.72	0.998	0.23	0.998
THL_Hypothalamus	10.47	0.082	2.53	0.899

P values were corrected for FDR

Inferior temporal outflows tended to be stronger in primates than in mouse, with rhesus macaques reaching the highest values at levels comparable to marmosets. Partner-level comparisons indicated that these primate advantages relative to mouse involved prefrontal and superior temporal targets, consistent with previously described circuits in the primate ventral visual stream [14–16]. When comparing humans with rhesus macaques, humans showed relatively lower striatal and amygdalar outflows while maintaining stronger insular outflows, pointing to a possible redistribution of temporal association influence away from subcortical partners and toward integrative cortico-cortical pathways. Thus, while rhesus showed the strongest ventral-stream–related outflows, humans may emphasize temporal–insula interactions within these pathways.

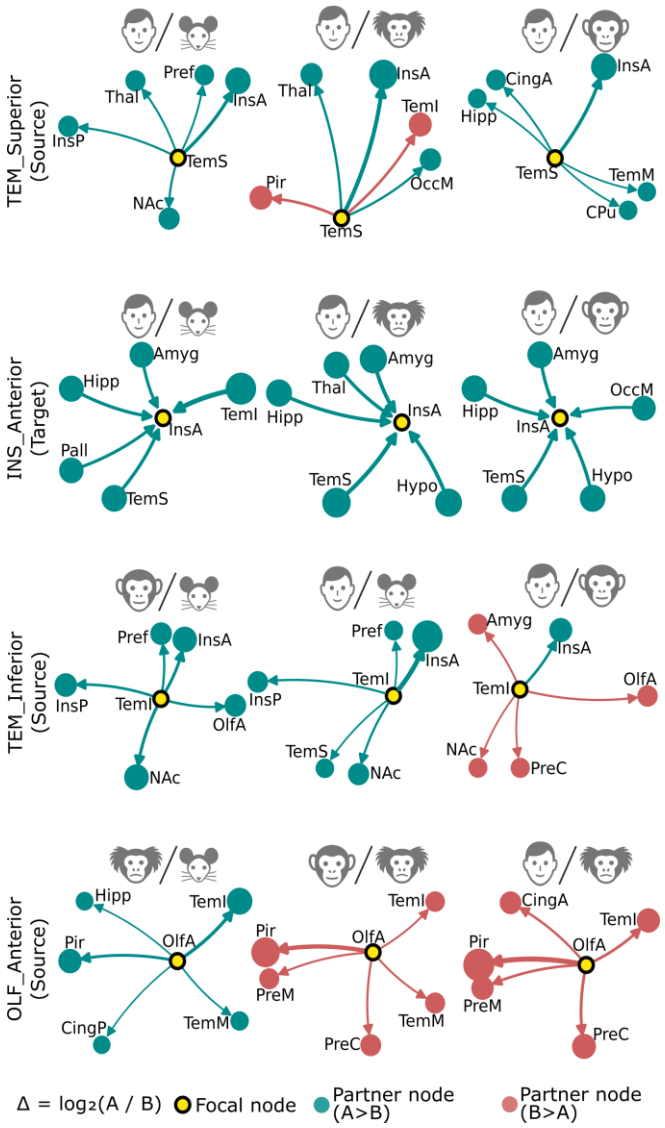

Figure 5 | Partner-specific contributions to regional role differences. Δ-connectomes illustrating partner-specific contributions to selected region–role differences (four representative rows). Each graph shows the focal region (center) and its top five partner regions ranked by |Δ|, with positions fixed across comparisons within a row for ease of tracking. Node size and edge width scale with |Δ|; edge direction reflects the focal role (source outflow vs. target inflow); node color indicates the sign of Δ (green = higher in the numerator species, red = higher in the denominator).

Olfactory roles showed the opposite trajectory, with the strongest efficiencies in marmoset and the weakest in humans (Fig. 4a–b). Partner-level differences revealed that marmoset vs. mouse contrasts reflected stronger anterior olfactory outflows to piriform and temporal regions. By contrast, marmoset vs. higher primates highlighted weaker anterior olfactory outflows to piriform, temporal, and frontal regions, consistent with a gradual reduction in olfactory influence in Old World primates and humans. Piriform inflows reinforced this pattern, with stronger inputs from olfactory and striatal regions in marmoset than in either rodents or higher primates.

Taken together, these results point to three domain-specific evolutionary trajectories: **(1)** human amplification of a temporal–insula–frontal circuit, potentially supporting multimodal integration and language-related functions[17–19]; **(2)** primate expansion of ventral visual stream pathways[20,21], peaking in rhesus macaques and possibly reorganized in humans toward insular integration; and **(3)** New World primate maintenance of relatively strong olfactory influence, consistent with chemosensory-based communication and ecological adaptation[22,23]. These domain-specific reallocations suggest that efficiency was differentially distributed across lineages, producing both human-associated gains and lineage-associated specializations.

3. Discussion:

3.1. Mouse Viral Tracer Integration and Cross-Species Directed Connectomes

A central challenge in comparative connectomics is that viral tract-tracing, the gold standard for determining projection directionality, remains practically and ethically restricted to mice and a few other small-brain species. Its invasive nature makes comprehensive application in humans or great apes impossible, leaving non-invasive diffusion MRI as the only feasible modality for large-brain primates. Diffusion tractography, however, is inherently symmetric: reconstructed streamlines yield bidirectional connectivity estimates, obscuring the unidirectional propagation of action potentials. This reciprocity limits the biological interpretability of dMRI-derived networks, especially in frameworks such as graph theory or dynamical systems modeling where directionality is essential[2,4].

Against this backdrop, our framework leverages the uniquely comprehensive viral tracing dataset in mouse (~1,200 injection experiments) as a directional scaffold, combined with species-specific dMRI-derived axonal lengths. This hybrid approach exploits the complementary strengths of both modalities: empirically validated projection asymmetries from tracing and whole-brain coverage from tractography. As shown in Fig. 3a and Supplementary Fig. 1, incorporating directionality stabilizes network organization across species. Randomizing tracer-defined directions causes networks to admit implausible detours and spurious shortcuts, generating extreme outliers and inflated path costs. By contrast, preserving true directionalities yields efficient and narrowly distributed cost profiles, even when paired with the wiring lengths of different species. These findings suggest that mouse-derived directionality provides a biologically meaningful constraint—one that anchors efficiency analyses across species, and without which the organizational structure would likely be severely disrupted.

Although based on mouse viral tracing, this integration provides precisely the directional constraint needed to uncover species-specific adaptations relative to a shared scaffold. What is introduced from the mouse is not its entire connectivity architecture, but only the empirically validated polarity of projections: the direction in which signals flow between regions. The spatial organization of white-matter trajectories, i.e. their lengths and embedding within each brain, is derived entirely from species-specific diffusion MRI, allowing us to examine how wiring constraints may have been shaped differently across lineages. By combining projection polarity from mouse tracing with species-specific axonal lengths, the framework makes it possible to reveal lineage-specific trade-offs: humans showed elevated efficiencies in long association pathways forming a temporal–insula–frontal circuit, rhesus macaques showed relative peaks in ventral visual outputs, and marmosets retained prominent olfactory–piriform influence (Figs. 4&5). In this way, directionality provides the missing constraint for path search, while each species' white-matter organization shapes a distinct efficiency landscape.

At present, there is no comprehensive alternative for defining directed human connectomes. Functional approaches such as dynamic causal modeling[3,24–26] have been widely applied to fMRI to infer directed connectivity, but their interpretation remains constrained by hemodynamic variability[27,28] across cortical regions. Differences in vascular dynamics introduce uncertainty in the temporal alignment of regional activation patterns, making causal interactions difficult to assess with rigor. Furthermore, causal relationships inferred from hemodynamic signals may not directly correspond to neuronal-level propagation[29–31], underscoring the need for structurally informed models that bridge scales. By grounding our networks in empirical structural asymmetries, we provide a biologically validated scaffold for directionality that avoids these pitfalls.

Importantly, the directed shortest paths identified in our models can be interpreted as routes of forward action potential propagation—minimal-cost sequences of axonal projections and synaptic

relays that maximize downstream impact per unit wiring investment. This framing bridges scales: the directed connectomes derived here are not statistical abstractions, but plausible mechanistic blueprints for how neuronal signals traverse large-scale networks. In turn, they provide a foundation for cross-species mechanistic modeling of cognition with spiking neural networks, where biologically grounded directional paths are essential for simulating signal flow, coherence, and emergent dynamics.

These cross-species directed connectomes provide structurally validated scaffolds for comparative inference. They point to evolutionary reallocations of efficiency, preserving canonical circuits such as the entorhinal–hippocampal pathway while exposing divergent shifts across sensory, associative, and limbic circuits. In the absence of any feasible alternative for whole-brain directed mapping in humans, this hybrid tracing–tractography framework offers a scalable platform for directed connectomics across species—one that not only enables evolutionary comparison but also constrains mechanistic models of large-scale brain dynamics[32].

3.2. Cross-Species Comparisons

A consistent finding across species was the high efficiency of the entorhinal–hippocampal pathway, which remained top-ranked in all connectomes (Fig. 3b). This preservation underscores how certain core circuits have been maintained through evolution, even as other systems appear to have been differentially emphasized. In contrast, lineage-specific reallocations of efficiency were also evident. For example, olfactory influence peaks in marmosets rather than mice, reflecting the strong chemosensory investment of New World primates and the relatively weaker association systems that may have allowed olfactory routes higher in the efficiency hierarchy. Rodents, by comparison, emphasize somatosensory systems, which may have reduced the relative prominence of olfactory pathways despite their absolute strength.

These contrasts highlight why evolutionary change is best interpreted in terms of relative prioritization rather than absolute wiring costs. Absolute path costs (axon length × inverse projection strength) can be size-corrected to enable interspecies comparison, but they primarily index the physical and metabolic expense of individual routes. In contrast, our rank-based efficiency situates each connectome within its own competitive landscape: shortest directed paths are ranked against all alternatives, so differences reflect shifts in network prioritization rather than absolute expense. This framing exposes trade-offs that absolute costs obscure: in humans, temporal–insula–frontal routes rise to the top while olfactory routes fall to the bottom; in marmosets, weaker association systems allow olfactory paths to occupy higher ranks; in rhesus macaques, ventral visual (inferior temporal) outputs peak without further human amplification. By integrating directionality with whole-network path search, the ranking captures how evolutionary pressures may have constrained influence hierarchies, identifying which circuits tend to be promoted or demoted, rather than only how long or strong individual edges are.

Taken together, our findings suggest that evolution reshaped cortical communication not through uniform scaling, but by reallocating efficiency across a balance of conserved core pathways and lineage-specific specializations. Humans showed elevated efficiency in a temporal–insula–frontal circuit, potentially supporting the integrative capacities underlying complex cognition and language[17–19]. Old World primates such as rhesus macaques exhibited high efficiency in ventral visual pathways, consistent with circuits for object and face recognition[20,21]. New World primates such as marmosets retained relatively strong olfactory influence, consistent with their reliance on chemosensory cues for social communication and ecological adaptation[22,23]. Alongside these divergent reallocations, conserved memory-related canonical projections, the entorhinal–hippocampal pathway[9,10] persisted across all species, anchoring the efficiency landscape. Together, these results indicate that cortical networks may have diversified through lineage-

specific peaks built alongside shared foundations, with humans, rhesus, and marmosets each representing distinct evolutionary solutions to the trade-offs imposed by expanding brain systems.

3.3. Limitations and Future Directions

Several limitations of this work should be acknowledged. First, projection polarity was derived exclusively from viral tracing in the mouse. While this dataset is uniquely comprehensive, it is possible that certain asymmetries are not conserved across species. We mitigated this by combining polarity with species-specific tractography, but future efforts that incorporate additional tracer resources in primates or new experimental modalities could further validate and refine the approach. Second, resolution differences between the common atlas and finer species-specific atlases impose constraints. Some structures, such as the claustrum or subthalamic nucleus, could not be reliably included, and the coarse common atlas resolution may obscure subfield-level specializations within regions like hippocampus or thalamus. Third, path efficiency emphasizes routing through shortest directed paths, but real neural dynamics can exploit redundant or parallel routes; complementary modeling approaches may provide a fuller account of interregional communication strategies.

Looking ahead, the integration of tracer-derived directionality with tractography offers several promising extensions. Higher-resolution parcellations, especially at the subnuclear level in limbic and thalamic systems, will enable more detailed analyses of intra-system organization. Additional cross-species tracer datasets, including ongoing work in marmoset and macaque, may allow polarity constraints to be derived directly within primates. Finally, coupling the directed connectomes with computational models, ranging from network control theory to spiking neural networks, could link the structural efficiency patterns observed here to functional dynamics and behavioral capacities.

4. Methods:

4.1. Neuroimaging Data and Processing

Diffusion MRI templates were constructed for human, rhesus macaque, marmoset, and mouse, each based on group-averaged datasets with species-appropriate acquisition and reconstruction parameters. For the human template, we used a total of 1,065 healthy adult scans acquired with a multi-shell diffusion scheme (b-values = 990, 1985, and 2980 s/mm²; 90 directions per shell)[33]. The in-plane resolution and slice thickness were 1.25 mm. Diffusion data were reconstructed using q-space diffeomorphic reconstruction[34], with restricted diffusion quantified using a model-free method[35]. Deterministic white matter fiber tracking[36] was applied, followed by trajectory-based tract recognition[37] and topology-informed pruning[38] to minimize false positives.

For the rhesus macaque template, we used 44 scans acquired with a multi-shell diffusion scheme (b-values = 500, 1000, and 2000 s/mm²; 6, 30, and 30 directions, respectively). Images were acquired at 1 mm isotropic resolution and resampled to 0.5 mm. Susceptibility distortions were corrected using TOPUP (Tiny FSL package, a re-compiled version of FSL TOPUP)[39], and b-tables were quality-checked by an automated routine[40]. Data were reconstructed in MNI space using generalized q-sampling imaging[41], with restricted diffusion quantified as above. Deterministic fiber tracking[36] with augmented tracking strategies[37] was employed to improve reproducibility.

For the marmoset template, we used 126 scans acquired with a multi-shell diffusion scheme (b-values = 1013 and 3019 s/mm²; 30 and 60 directions, respectively). The in-plane resolution was 0.35 mm with a slice thickness of 0.7 mm, and images were resampled to 0.20 mm isotropic. Diffusion data were reconstructed in MNI space using q-space diffeomorphic reconstruction[34] to obtain spin distribution functions[41], with a diffusion sampling length ratio of 1.25 and an output resolution of 0.20 mm isotropic. Restricted diffusion was quantified using restricted diffusion imaging[35].

For the mouse template, we used 22 C57BL/6 brains acquired at ultra-high resolution (0.025 mm isotropic) with a single-shell HARDI sequence (b = 3000 s/mm²; 114 directions). Diffusion data were reconstructed in MNI space using q-space diffeomorphic reconstruction[34] to obtain spin distribution functions[41], with an output resolution of 0.025 mm isotropic. Tractography was performed using deterministic fiber tracking[36] with augmented tracking strategies[37].

All templates were aligned to standard stereotaxic coordinate systems, reconstructed using consistent model-free approaches, and processed with deterministic tractography, ensuring comparability across species.

4.2. Mouse Viral Tracer Integration and Directed Path Modeling

4.2.1. Viral Tracer Data and Preprocessing

We used a publicly available mouse mesoscale connectome dataset[1] comprising 1,199 anterograde viral tracing injection experiments reported in the Allen Mouse Brain Connectivity Atlas database. For each experiment, both injection density and projection density volumes were downloaded in NRRD format via the Allen Brain Atlas API (http://api.brain-map.org/), converted to NIfTI, and spatially registered to the mouse diffusion MRI space using rigid and nonlinear transformations. Two experiments contained no labeled voxels and were excluded from analysis, leaving 1,197 injections for computation. Volumes were binarized to remove floating-point artifacts, yielding binary masks of injection and projection coverage. All tracer and tractography data were mapped to a previously developed common hierarchical atlas that defines 22 homologous cortical and subcortical regions across species (see companion paper[6]). This ensured one-to-one correspondence of ROIs for integration and comparison.

4.2.2. Estimation of Directed Projection Strengths

Let A be the atlas label volume (*0* = background; *1…R* = region IDs), S_k the binarized injection mask for experiment k, and P_k the binarized projection mask for the same experiment. The indicator function $1[.]$ equals 1 if the condition holds and 0 otherwise.

Injection fraction for region i (experiment k):

$$f_i^{inj,k} = \frac{\sum_x 1[A(x) = i]\, 1[S_k(x) = 1]}{\sum_x 1[S_k(x) = 1]} \quad (1)$$

Here $f_i^{inj,k}$ denotes the fractional coverage of source region i by experiment k; experiments with partial injections contribute proportionally to their coverage, while zero-coverage cases contribute nothing. This ensures that directed strengths are weighted by the effective fraction of each region covered by the injection. Projection fraction for region j (experiment k):

$$f_j^{proj,k} = \frac{\sum_x 1[A(x) = j]\, 1[P_k(x) = 1]}{\sum_x 1[P_k(x) = 1]} \quad (2)$$

Experiment-level weight from $i \to j$:

$$w_{i\to j}^{(k)} = f_i^{inj,k}\, f_j^{proj,k} \quad (3)$$

Final directed projection matrix (sum over valid experiments; $N = 1197$):

$$\mathrm{DirMat}_{i,j} = \sum_{k=1}^{N} w_{i\to j}^{(k)} = \sum_{k=1}^{N} f_i^{inj,k}\, f_j^{proj,k} \quad (4)$$

This procedure allocates each experiment's injected signal across source regions ($f_i^{inj,k}$) and its projection signal across target regions ($f_j^{proj,k}$), then form a sum of outer products across experiments to estimate directed strengths $i \to j$ in atlas space. Background voxels ($A = 0$) are excluded from all sums. Thus, the final directed matrix represents a coverage-weighted sum across all experiments, reducing bias from incomplete tracer injections.

For the fine-scale mouse analysis, the same computation is performed in Allen Brain Atlas (ABA) space. For the cross-species analysis, the directed strengths computed in the mouse MRI atlas space (common atlas version) are subsequently integrated with species-specific diffusion MRI connectivity to derive *effective connection costs* and *path efficiencies*.

4.2.3. Diffusion MRI Connectivity

For each species (mouse, marmoset, rhesus macaque, human), diffusion MRI tractography was performed to generate a species-specific undirected connectivity matrix of mean axonal lengths[5,42] $L_{ij} = L_{ji}$ between all common atlas region pairs. Mean lengths were expressed in millimeters and computed only for region pairs with a nonzero number of streamlines. Tractography was performed using whole brain seeding. For the mouse brain, the tractography output was mapped to the same diffusion MRI atlas space used for registering the viral tracer data, ensuring voxel-level correspondence for subsequent multimodal integration.

4.2.4. Integration of Modalities into Effective Connection Cost Matrices

Mouse-derived directed projection strengths $DirMat_{i,j}$ in common atlas space were applied to the dMRI-derived axonal lengths L_{ij} for each species to compute the *effective connection cost*:

$$\mathrm{EffCost}_{i\to j} = \begin{cases} \dfrac{L_{ij}}{\sqrt[3]{V}.\,\mathrm{DirMat}_{i,j}}, & if\ \mathrm{DirMat}_{i,j} > 0\ and\ L_{ij} > 0, \\ 0, & \text{otherwise.} \end{cases} \quad (5)$$

where V is the total white matter volume of the species (in mm^3), used to normalize for brain size. A connection was defined only if both modalities supported it (nonzero $\mathrm{DirMat}_{i,j}$and nonzero L_{ij}), reducing false positives from spurious tractography streamlines or tracer noise. Although axonal length is symmetric, $\mathrm{EffCost}_{i\to j} \neq \mathrm{EffCost}_{j\to i}$ because $\mathrm{DirMat}_{i,j}$ encodes directional projection strength.

Effective connection cost reflects the physical and metabolic investment required per unit of potential influence between two regions. For connections of equal length, a stronger projection yields a lower effective cost because it offers more potential influence per unit wiring investment. In contrast, weak projections of the same length are metabolically more wasteful, sustaining the same infrastructure for reduced influence yield.

Effective connection cost matrices were computed between homologous common-atlas ROIs across species. This set reflects specific consolidations necessitated by species-specific anatomical resolution: (i) Because the mouse atlas lacks parietal lobe subdivisions, we retained an undivided PAR region for all species (Level-1 definition for Parietal Lobe), (ii) In primates, the caudate and putamen were merged into a single BG_CaudoPutamen ROI to match the undivided form in rodents. These ROI definitions follow the constraints of the common atlas, ensuring consistency across species. With these constraints, the number of valid directed paths is 22×21=462. These same ROI definitions were used in all downstream path efficiency analyses, including the path-level ranking and regional-level comparisons.

4.2.5. Path Efficiency Analysis

Minimum path costs between all region pairs were computed from the effective connection cost network as the lowest cumulative cost along any valid directed route, using a shortest directed path algorithm[43].

$$\mathrm{PathCost}_{i\to j} = \min_{p_{i\to j}} \sum_{(u\to v)\in p_{i\to j}} \mathrm{EffCost}_{u\to v} \quad (6)$$

where $p_{i\to j}$ is any directed path (sequence of directed edges) from region i to j. Only edges with nonzero mapped projection strengths ($\mathrm{DirMat}_{u,v} > 0$) were considered valid in the path search.

Wiring minimization alone may lack the explanatory power to fully account for the complex topology of the mouse brain connectome[43]. In the current study, the minimization function is multi-objective, combining axonal length and the inverse of projection density. This favors shorter axons with stronger projections, yielding directed shortest paths that are simultaneously length-minimizing and projection-strength–maximizing.

Biologically, these minimal-cost directed paths approximate the forward propagation of action potentials from source to target through the most efficient influence channels. They represent sequences of axonal projections and synaptic relays that minimize wiring investment while maximizing potential impact, providing a mechanistic basis for modeling large-scale cortical dynamics.

4.3. Cross-species Comparisons

4.3.1. Cross-species Path Efficiency Ranking

To compare path efficiency across species, we ranked all valid inter-regional paths by their minimum path cost, with lower-cost paths receiving higher ranks. We then computed an inverse-rank efficiency score, $1/R_{i\to j}^{(s)}$, for species s, providing a normalized measure that allows comparison across species with different brain sizes and network scales. Since most paths have relatively low efficiency and the score distribution is right-skewed, a monotonic log transformation was applied for visualization purposes to expand the mid-range values and improve clarity in plots. However, this transformation was not used in subsequent Δ-connectome calculations.

4.3.2. Regional-Level Statistical Comparisons

While all valid directed paths (n=462) were assigned efficiency ranks (see Methods, Path efficiency analysis), formal cross-species comparisons were performed at the regional level, treating each region separately in its role as a source (outgoing edges) or target (incoming edges). These analyses used the same 22 homologous ROIs defined for the effective connection cost matrices, ensuring one-to-one correspondence across species.

For a given region–role combination, we extracted the efficiency values of all valid paths in which that region served in the specified role, yielding one distribution per species. We then applied a Kruskal–Wallis test to assess whether distributions differed among species. When significant, we performed pairwise post hoc Dunn's tests with false discovery rate (FDR) correction.

This approach reduces the number of statistical tests by evaluating distributions of all paths linked to a region rather than testing each path independently. While low-efficiency connections still contribute to the analysis, they are interpreted in aggregate alongside higher-efficiency connections from the same region, shifting the emphasis from isolated edges to anatomically coherent loci of potential divergence. This prioritizes direct anatomical interpretability and focuses on evolutionarily meaningful patterns that can be related to known structural and functional roles.

4.3.3. Δ-Connectome Visualization

For each region–role combination included in the analysis, we identified all valid directed paths in which the region served in the specified role (Source or Target). For each path, we computed the log_2 ratio of efficiency (E) between two species:

$$\Delta_{u\to v} = log_2\left(\frac{E_{u\to v}^{(sp_1)}}{E_{u\to v}^{(sp_2)}}\right) \quad (7)$$

where sp_1 and sp_2 denote the two species being compared. Positive values indicate higher efficiency in sp_1; negative values indicate higher efficiency in sp_2.

For each partner region connected to the focal region, we averaged Δ values across all relevant paths and retained the top partners ranked by absolute mean delta. A directed subgraph was then constructed with the focal region and its top partners as nodes, edge directions determined by

the focal role, node size proportional to |Δ|, node color indicating the sign of Δ, and edge width proportional to |Δ|. Graphs were arranged using a modified circular layout with the focal region centered.

Acknowledgments
Computational resources were provided by the Pittsburgh Supercomputing Center through NSF ACCESS allocations MED230052 and CIS200026.

Use of AI Tools
ChatGPT (OpenAI) was employed to aid in language refinement and to suggest initial code structures for figure visualizations. All code related to data analysis and modeling was written exclusively by the authors, who take full responsibility for all scientific content, code implementation, and conclusions.

Author Contributions
Siva Venkadesh: Conceptualization, Methodology (viral tracer integration, dMRI tractography, network modeling), Formal analysis, Software, Validation, Visualization, Writing – Original Draft, Writing – Review & Editing, Supervision
Yuhe Tian: Software, Visualization
Wen-Jieh Linn: Data Curation, Visualization
G. Allan Johnson: Conceptualization, Methodology (viral tracer integration), Writing – Review & Editing, Study oversight, Resources, Funding acquisition.
Fang-Cheng Yeh: Conceptualization, Methodology (dMRI tractography), Writing – Review & Editing, Study oversight, Resources, Funding acquisition.

Funding
This work was supported by the National Institutes of Health grant R01NS120954. SV was supported in part by NIH grant R01MH134004.

Competing Interests
The authors declare no competing interests.

Data and Code Availability
The present bioRxiv version does not include extended supplementary materials or data release. A future version will include full supplementary information along with open access to processed data and code supporting the analyses reported here.

REFERENCES

1. Oh, S. W. *et al*. A mesoscale connectome of the mouse brain. *Nature* 508, 207–214 (2014).
2. Kale, P., Zalesky, A. & Gollo, L. L. Estimating the impact of structural directionality: How reliable are undirected connectomes? *Netw Neurosci* 2, 259–284 (2018).
3. Seguin, C., Razi, A. & Zalesky, A. Inferring neural signalling directionality from undirected structural connectomes. *Nat. Commun*. 10, 4289 (2019).
4. Bullmore, E. & Sporns, O. Complex brain networks: graph theoretical analysis of structural and functional systems. *Nat. Rev. Neurosci.* 10, 186–198 (2009).
5. Latora, V. & Marchiori, M. Efficient behavior of small-world networks. *Phys. Rev. Lett.* 87, 198701 (2001).
6. Venkadesh S, et al. A common cross-species atlas of cortical gray matter. *In Submission* (2025).
7. Calabrese, E., Badea, A., Cofer, G., Qi, Y. & Johnson, G. A. A Diffusion MRI Tractography Connectome of the Mouse Brain and Comparison with Neuronal Tracer Data. *Cereb. Cortex* 25, 4628–4637 (2015).
8. Yeh, F.-C. *DSI Studio*. (2021). doi:10.5281/zenodo.4978980.
9. Buzsáki, G. & Moser, E. I. Memory, navigation and theta rhythm in the hippocampal-entorhinal system. *Nat. Neurosci.* 16, 130–138 (2013).
10. Moser, M.-B., Rowland, D. C. & Moser, E. I. Place cells, grid cells, and memory. *Cold Spring Harb. Perspect. Biol.* 7, a021808 (2015).
11. Witter, M. P., Doan, T. P., Jacobsen, B., Nilssen, E. S. & Ohara, S. Architecture of the entorhinal cortex A review of entorhinal anatomy in rodents with some comparative notes. *Front. Syst. Neurosci.* 11, 46 (2017).
12. Amaral, D. G. & Witter, M. P. The three-dimensional organization of the hippocampal formation: a review of anatomical data. *Neuroscience* 31, 571–591 (1989).
13. Ishizuka, N., Weber, J. & Amaral, D. G. Organization of intrahippocampal projections originating from CA3 pyramidal cells in the rat. *J. Comp. Neurol.* 295, 580–623 (1990).
14. Kravitz, D. J., Saleem, K. S., Baker, C. I., Ungerleider, L. G. & Mishkin, M. The ventral visual pathway: an expanded neural framework for the processing of object quality. *Trends Cogn. Sci.* 17, 26–49 (2013).
15. DiCarlo, J. J., Zoccolan, D. & Rust, N. C. How does the brain solve visual object recognition? *Neuron* 73, 415–434 (2012).
16. Saleem, K. S., Suzuki, W., Tanaka, K. & Hashikawa, T. Connections between anterior inferotemporal cortex and superior temporal sulcus regions in the macaque monkey. *J. Neurosci.* 20, 5083–5101 (2000).
17. Menon, V. Insular cortex: A hub for saliency, cognitive control, and interoceptive awareness. in *Encyclopedia of the Human Brain* 159–183 (Elsevier, 2025).
18. Binder, J. R., Desai, R. H., Graves, W. W. & Conant, L. L. Where is the semantic system? A critical review and meta-analysis of 120 functional neuroimaging studies. *Cereb. Cortex* 19, 2767–2796 (2009).
19. Friederici, A. D. The brain basis of language processing: from structure to function. *Physiol. Rev.* 91, 1357–1392 (2011).
20. Lafer-Sousa, R. & Conway, B. R. Parallel, multi-stage processing of colors, faces and shapes in macaque inferior temporal cortex. *Nat. Neurosci.* 16, 1870–1878 (2013).
21. Eldridge, M. A. G. *et al*. Visual recognition in rhesus monkeys requires area TE but not TEO. *Cereb. Cortex* 33, 3098–3106 (2023).

22. Lazaro-Perea, C., Snowdon, C. T. & de Fátima Arruda, M. Scent-marking behavior in wild groups of common marmosets (Callithrix jacchus). *Behav. Ecol. Sociobiol.* 46, 313–324 (1999).
23. Kemp, C. & Kaplan, G. Facial expressions in common marmosets (Callithrix jacchus) and their use by conspecifics. *Anim. Cogn.* 16, 773–788 (2013).
24. Friston, K. J., Harrison, L. & Penny, W. Dynamic causal modelling. *Neuroimage* 19, 1273–1302 (2003).
25. Park, H.-J., Friston, K. J., Pae, C., Park, B. & Razi, A. Dynamic effective connectivity in resting state fMRI. *Neuroimage* 180, 594–608 (2018).
26. Frässle, S. *et al.* Whole-brain estimates of directed connectivity for human connectomics. *Neuroimage* 225, 117491 (2021).
27. Handwerker, D. A., Ollinger, J. M. & D'Esposito, M. Variation of BOLD hemodynamic responses across subjects and brain regions and their effects on statistical analyses. *Neuroimage* 21, 1639–1651 (2004).
28. West, K. L. *et al.* BOLD hemodynamic response function changes significantly with healthy aging. *Neuroimage* 188, 198–207 (2019).
29. Hoel, E. P., Albantakis, L. & Tononi, G. Quantifying causal emergence shows that macro can beat micro. *Proc. Natl. Acad. Sci. U. S. A.* 110, 19790–19795 (2013).
30. Hoel, E. P., Albantakis, L., Marshall, W. & Tononi, G. Can the macro beat the micro? Integrated information across spatiotemporal scales. *Neurosci Conscious* 2016, niw012 (2016).
31. Marshall, W., Albantakis, L. & Tononi, G. Black-boxing and cause-effect power. *PLoS Comput. Biol.* (2018).
32. Venkadesh, S. & Van Horn, J. D. Integrative Models of Brain Structure and Dynamics: Concepts, Challenges, and Methods. *Front. Neurosci.* 15, 752332 (2021).
33. Van Essen, D. C. *et al.* The WU-Minn Human Connectome Project: an overview. *Neuroimage* 80, 62–79 (2013).
34. Yeh, F.-C. & Tseng, W.-Y. I. NTU-90: a high angular resolution brain atlas constructed by q-space diffeomorphic reconstruction. *Neuroimage* 58, 91–99 (2011).
35. Yeh, F.-C., Liu, L., Hitchens, T. K. & Wu, Y. L. Mapping immune cell infiltration using restricted diffusion MRI. *Magn. Reson. Med.* 77, 603–612 (2017).
36. Yeh, F.-C., Verstynen, T. D., Wang, Y., Fernández-Miranda, J. C. & Tseng, W.-Y. I. Deterministic diffusion fiber tracking improved by quantitative anisotropy. *PLoS One* 8, e80713 (2013).
37. Yeh, F.-C. Shape analysis of the human association pathways. *Neuroimage* 223, 117329 (2020).
38. Yeh, F.-C. *et al.* Automatic Removal of False Connections in Diffusion MRI Tractography Using Topology-Informed Pruning (TIP). *Neurotherapeutics* 16, 52–58 (2019).
39. Jenkinson, M., Beckmann, C. F., Behrens, T. E. J., Woolrich, M. W. & Smith, S. M. FSL. *Neuroimage* 62, 782–790 (2012).
40. Schilling, K. G. *et al.* A fiber coherence index for quality control of B-table orientation in diffusion MRI scans. *Magn. Reson. Imaging* 58, 82–89 (2019).
41. Yeh, F.-C., Wedeen, V. J. & Tseng, W.-Y. I. Generalized q-sampling imaging. *IEEE Trans. Med. Imaging* 29, 1626–1635 (2010).
42. Hagberg, A., Swart, P. & S Chult, D. *Exploring Network Structure, Dynamics, and Function Using NetworkX*. https://www.osti.gov/biblio/960616-exploring-network-structure-dynamics-function-using-networkx (2008).
43. Rubinov, M., Ypma, R. J. F., Watson, C. & Bullmore, E. T. Wiring cost and topological participation of the mouse brain connectome. *Proc. Natl. Acad. Sci. U. S. A.* 112, 10032–10037 (2015).

Supplementary Material

Supplementary Table – 1. Symbol Reference for Equations

Symbol	Definition	Type / Units
Atlas and Masks		
$A(x)$	Atlas label at voxel x (0 = background, 1…R = region IDs)	integer
$S_k(x)$	Injection mask for experiment k (binary: 1 = injected voxel, 0 = otherwise)	binary
$P_k(x)$	Projection mask for experiment k (binary: 1 = projected voxel, 0 = otherwise)	binary
1[·]	Indicator function: 1 if condition is true, else 0	binary
Region-Level Fractions		
$f_i^{inj,k}$	Injection fraction for region i in experiment k (Eq. 1)	unitless
$f_j^{proj,k}$	Projection fraction for region j in experiment k (Eq. 2)	unitless
Directed Strengths		
$w_{i\to j}^{(k)}$	Experiment-level directed strength from i to j in experiment k (Eq. 3)	unitless
$\mathrm{DirMat}_{i,j}$	Final directed projection strength from i to j, summed over all experiments (Eq. 4)	unitless
Diffusion MRI Measures		
$L_{ij} = L_{ji}$	Mean axonal length between regions i and j from tractography	mm
V	Total white matter volume for species	mm^3
Effective Costs and Paths		
$\mathrm{EffCost}_{i\to j}$	Effective connection cost from i to j (Eq. 5)	mm / mm
$\mathrm{PathCost}_{i\to j}$	Minimum path cost between i and j (Eq. 6)	mm / mm
$p_{i\to j}$	Directed path (sequence of edges) from i to j	set of ordered pairs

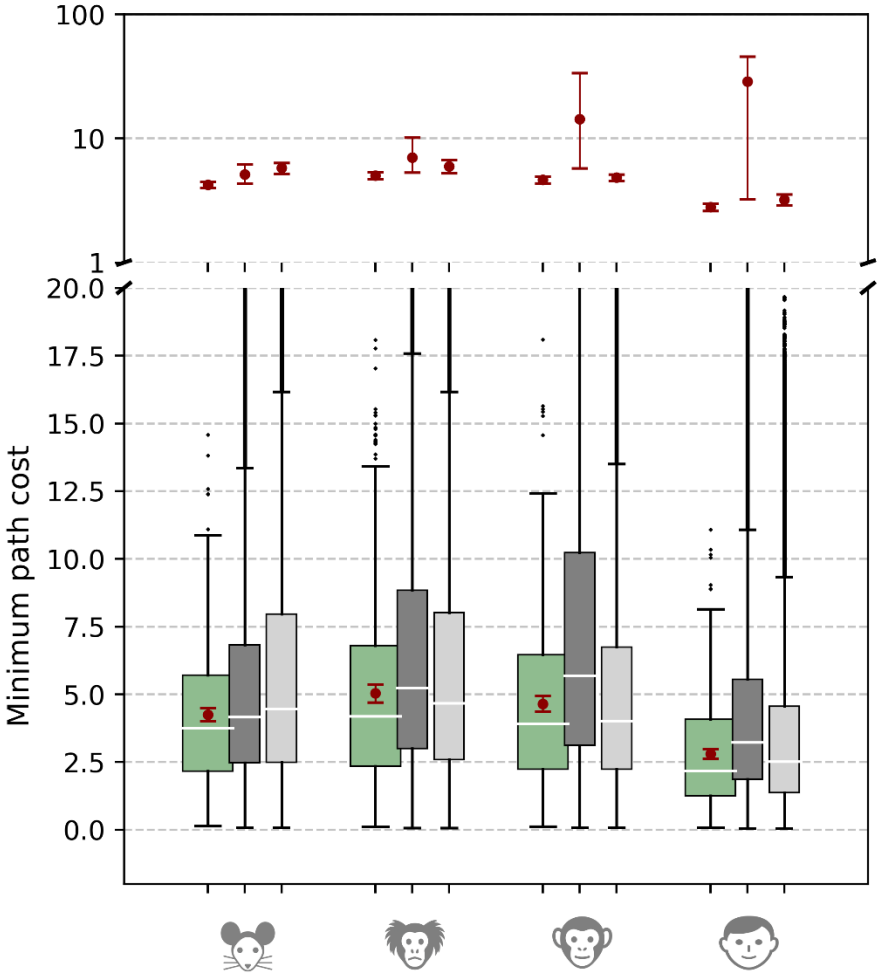

Supplementary Figure 1 | Path cost distributions for real connectomes (green) and null networks from 10,000 permutations, shown as the full 462 × 10,000 distributions to illustrate the spread of nulls. Both tracer-directionality shuffles (dark grey) and dMRI-length shuffles (light grey) are shown. Mean path cost (± SD) across null permutations and the corresponding real mean: Mouse: real = 4.25, tracer-shuffle = 5.15 ± 0.48, dMRI-shuffle = 5.79 ± 0.29; Marmoset: real = 5.04, tracer-shuffle = 7.02 ± 1.92, dMRI-shuffle = 5.96 ± 0.38; Rhesus: real = 4.65, tracer-shuffle = 14.27 ± 45.9, dMRI-shuffle = 4.85 ± 0.15; Human: real = 2.80, tracer-shuffle = 28.7 ± 661.6, dMRI-shuffle = 3.21 ± 0.17. Tracer-randomized nulls showed far greater spread than dMRI-length–randomized nulls, underscoring the stabilizing influence of directionality on network organization. Without directional constraints, networks admitted inefficient detours and spurious shortcuts, generating extreme path costs. In contrast, randomizing axonal lengths raised overall costs but retained narrower distributions, consistent with directionality anchoring efficient routes even under altered wiring distances.

Supplementary Table – 2. Pairwise Species Comparisons of Regional Efficiency Using Dunn's Test

Comparison	Z-score	*P*
TEM_Inferior (Source)		
Mouse vs Marmoset	**-3.05**	0.007
Mouse vs Rhesus	**-3.36**	0.005
Mouse vs Human	-1.58	0.170
Marmoset vs Rhesus	-0.31	0.757
Marmoset vs Human	1.47	0.170
Rhesus vs Human	1.78	0.150
TEM_Superior (Source)		
Mouse vs Marmoset	0.03	0.972
Mouse vs Rhesus	-1.05	0.352
Mouse vs Human	**-3.03**	0.007
Marmoset vs Rhesus	-1.08	0.352
Marmoset vs Human	**-3.07**	0.007
Rhesus vs Human	-1.98	0.095
INS_Anterior (Source)		
Mouse vs Marmoset	**3.98**	0.000
Mouse vs Rhesus	0.91	0.362
Mouse vs Human	-1.8	0.086
Marmoset vs Rhesus	**-3.06**	0.004
Marmoset vs Human	**-5.78**	0.000
Rhesus vs Human	**-2.71**	0.010
INS_Anterior (Target)		
Mouse vs Marmoset	2.05	0.061
Mouse vs Rhesus	0.43	0.669
Mouse vs Human	**-3.01**	0.005
Marmoset vs Rhesus	-1.62	0.126
Marmoset vs Human	**-5.06**	0.000
Rhesus vs Human	**-3.43**	0.002
OLF_Anterior (Source)		
Mouse vs Marmoset	-0.92	0.356
Mouse vs Rhesus	1.51	0.157
Mouse vs Human	**3.03**	0.007
Marmoset vs Rhesus	**2.44**	0.030
Marmoset vs Human	**3.95**	0.001
Rhesus vs Human	1.52	0.157
OLF_Piriform (Target)		
Mouse vs Marmoset	**-3.07**	0.004
Mouse vs Rhesus	1.58	0.136
Mouse vs Human	1.88	0.090
Marmoset vs Rhesus	**4.66**	0.000
Marmoset vs Human	**4.96**	0.000
Rhesus vs Human	0.3	0.766

p-values were corrected for FDR.